Granular Matter
DOI 10.1007/s10035-013-0478-9

ORIGINAL PAPER

Single particle contact versus particle packing behavior: model based analysis of chemically modified glass particles

Katja Mader-Arndt · Zinaida Kutelova · Regina Fuchs · Jan Meyer · Thorsten Staedler · Werner Hintz · Jürgen Tomas

Received: 28 February 2013
© Springer-Verlag Berlin Heidelberg 2014

Abstract Smooth spherical micro glass particles are the reference particle system to demonstrate the correlation between single contacts and the particle packing properties. To investigate the influence of the van der Waals attraction force, the particles will be functionalized to obtain hydrophilic and hydrophobic surfaces. To remove the impurities and hydrophilize the particle surfaces a very strong oxidizing agent is used—the peroxymonosulfuric acid. In order to generate a hydrophobic glass surface, the process of silanization is applied. The comprehensive force displacement model of elastic-plastic and adhesive contacts are discussed. Therefore the model 'stiff particles with soft contacts' is used to quantify and compare the elastic-plastic contact properties. In this work, the particle contacts are experimentally investigated by means of atomic force microscopy (AFM), nanoindentation and shear tests. While the AFM and nanoindenter measurements are aimed to analyse single particle contacts, shear tests are used for particle packing studies. The fundamental challenge and question is addressed and answered: How do the micro mechanical material properties change when the glass surfaces are functionalized? Do we obtain the same behavior for the used micro glass particles when we compare the different methods?

Keywords Van der Waals attraction force · Surface functionalization · Particle contact · Powder bulk behavior

K. Mader-Arndt (✉) · Z. Kutelova · W. Hintz · J. Tomas
Institute for Process Engineering, Mechanical Process Engineering, Otto von Guericke University Magdeburg, Universitätsplatz 2, 39106 Magdeburg, Germany
e-mail: katja.mader@ovgu.de

R. Fuchs · J. Meyer · T. Staedler
Institute of Materials Engineering, Surface and Materials Technology, University of Siegen, Paul-Bonatz-Straße 9-11, 57076 Siegen, Germany

List of symbols

a_0	Minimum molecular surface distance (nm)
C_H	Hamaker constant (J)
γ	Surface energy (mJ/m^2)
γ_D	Surface energy dispersive fraction (mJ/m^2)
γ_P	Surface energy polar fraction (mJ/m^2)
d	Particle diameter (μm)
E	Effective modulus of elasticity (kN/mm^2)
ff_c	Flow function ($-$)
F_G	Gravitational force (nN)
F_H	Adhesion force (in general) (μN)
F_{H0}	Adhesion force of contact point (nN)
F_N	Normal force (μN)
$F_{N,Y}$	Normal force at yield point (nN)
h_K	Displacement (nm)
$h_{K,Y}$	Displacement at yield point (nm)
$k_{N,el-pl}$	Elastic-plastic contact stiffness (N/m)
κ	Contact consolidation coefficient ($-$)
κ_A	Elastic-plastic contact surface ratio ($-$)
κ_p	Plastic repulsion coefficient ($-$)
p_f	Micro-yield strength (MPa)
p_{VdW}	van der Waals bond stress (MPa)
$r_{1,2}$	Effective particle radius (nm)
$r_{K,el}$	Elastic contact radius (nm)
W_{diss}	Energy absorption or dissipation (Nm)
ρ	Density (g/cm^3)
ρ_b	Bulk density (g/cm^3)
σ	Normal stress (Pa)
σ_c	Uniaxial compressive strength (Pa)
σ_0	Isostatic tensile strength (Pa)
σ_1	Major principal stress (Pa)
σ_{pre}	Preshear stress (Pa)
τ	Shear stress (Pa)
φ_i	Angle of internal friction (°)

Published online: 19 January 2014

φ_e Effective angle of internal friction (°)
φ_{st} Stationary angle of internal friction (°)

1 Introduction

In the last years various nano- and microscale materials have been interesting for many applications. In terms of the flow properties of such bulk materials, one can find that cohesive and compressible powders consist of fine (particle size $d < 100\,\mu m$), ultrafine ($d < 10\,\mu m$) or nanosized ($d < 1\,\mu m$) particles [1]. For applications e.g. in pharmaceutics and food industry, the flow properties are important with regard to the product design, conveying, packing or transport. Due to the higher specific surface areas and the decreasing contact stiffness of nanodispersed particles, the effect of adhesion becomes strong. In case of fine, dry nanoparticles, the adhesion is the van der Waals attraction force [2,3]. Most of the handling problems are caused by undesired adhesion with sticking or cementing of the conveyed and stored products. On the other hand, adhesion can be desirable, e.g. in pharmaceutics, to improve the product quality by processes like agglomeration, formulation (tablet press) or particle coatings [4]. These desirable effects are because of the fact that the interparticular adhesion forces, especially the van der Waals attraction forces F_{H0}, exceed the gravitational forces F_G of the particles by several orders of magnitude (see Table 1) [4,5]. One of the scientific and industrial challenges is the trouble-free handling of cohesive powders.

On the basis of the dimensionless elastic-plastic contact consolidation coefficient κ, the approximated linear adhesion force intensification $F_H(F_N)$ of particles by contact flattening, can be evaluated (see Table 2). This results from a preloading with a normal load F_N [6]. A stiff contact behavior with pronounced low adhesion ability is characterized by values of the contact consolidation coefficient

$\kappa = 0 - 0.1$ and consequently $F_H \approx F_{H0}$. Respectively, with increasing flattening the contact stiffness decreases κ and the adhesion force F_H increase. The contact point is deformed to contact area with increasing adhesion potential. Macroscopically this effect is experienced by the load dependent increase of the compressive strength and the shear resistance of fine dispersed cohesive powders. This process is known as pre-consolidation. Since this behavior is typical for the consolidation of dry, fine, adhesive particle systems, the crucial influence of the load dependent adhesion force must be microscopically evaluated. The respective description of this coefficient can be read in Sect. 4.1.

The scope of the present work is to build a bridge between the 'microscopic' particle properties and the 'macroscopic' mechanical behavior of cohesive bulk materials, on the basis of an elastic-plastic contact model with variable adhesion.

As a model system in the present paper, cohesive micro glass particles, whose surface properties were chemically modified, are used. The chemical modification implies particle hydrophilization and hydrophobization. The creation of a hydrophobic glass surface is possible by means of the so-called silanization process, which has been used for decades to modify the surface of silica and other materials [7].

The macroscopic or continuum powder behavior of surface modified glass beads were assessed with shear tests, and

Table 1 Adhesiveness of fine, dry particles [4,5]

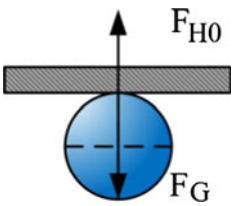
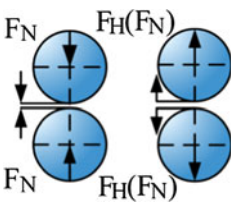
	Particle size d (μm)	Ratio F_{H0}/F_G	Evaluation
	10–100	$1–10^2$	Slightly adhesive
	1–10	$10^2–10^4$	Adhesive
	0.01–1	$10^4–10^8$	Very adhesive

Table 2 Evaluation of the adhesion force intensification $F_H(F_N)$ [4]

	Particle size d (μm)	Contact consolidation coefficient κ	Evaluation of contact behavior
	1–100	0.1–0.3	Soft
	0.1–1	0.3–0.8	Very soft
	0.01–0.1	>0.8	Extremely soft

microscopic contact properties were measured by AFM and nanoindentation.

2 Model for 'stiff particles with soft contacts'

In the proposed model, the external forces and short-range adhesion forces contribute towards a localized contact deformation. The contact areas are small in comparison to the particle size. Therefore only the contact forces and the direct response behavior, i.e. the approach of the centers of two contact partners, are considered. The model is characteristic for the particle contact with variable adhesion and considers the adhesive, elastic-plastic and viscous, elastic-plastic contact deformation with the unloading and reloading hysteresis as well as the energy absorption [1].

2.1 Normal force: displacement function with variable adhesion

The first fundamental of the elastic contact compression under normal loading was developed by Hertz [8]. With the approach of the elliptical stress distribution across the contact area, Hertz derived the nonlinear elastic normal force-displacement law for isotropic smooth particles. The principal stresses within and outside the contact area were introduced by Huber [9]. Examples for analytical and numerical models of the spatial stress distribution within a sphere were given by Lurje [10]. An additional contribution to the normal force by a constant adhesion of the elastic contact was observed e.g. by Sperling [11], Derjaguin et al. [12,13], Dahneke [14,15], Johnson et al. [16,17], Greenwood [18] and Götzinger [19], Zhou and Peukert [20] and Li et al. [21].

For the production and handling of fine particles it is necessary to consider the fact of variable adhesion because of the van der Waals attraction forces between particles. The interactions between the plastic and viscoplastic contact deformation and the increasing adhesion with plastic deformation and not contact flattening are not investigated extensively in the literature. Therefore, analytical functions of the normal force-displacement behavior are shown which considered step-wise transitions from the elastic, elastic-plastic and fully plastic contact behavior with a constant flow pressure (yield limit) and a variable adhesion force, which depends on the contact flattening.

Figure 1 shows the normal force-displacement behavior of a particle-particle contact, according to Tomas [1].

After the approach (1) from an infinite distance to a minimum separation the two spherical contact partners are in direct contact with a molecular minimum distance a_0. This surface distance can be calculated for van der Waals attraction and Born repulsion as first derivative of molecular Lennard-Jones potential setting equivalent to zero. At this point a

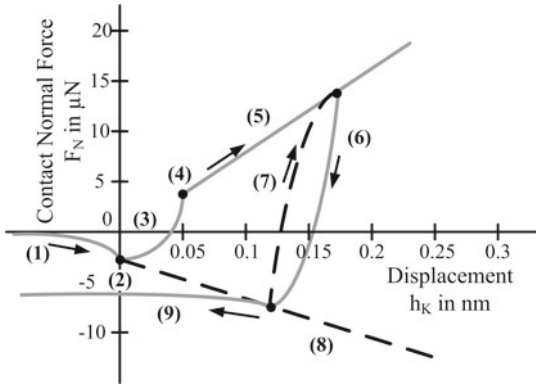


Fig. 1 Characteristic normal force-displacement behavior of two smooth isotropic particles

smooth sphere-sphere contact without any contact deformation ($h_K = 0$) is formed by the negative short range attractive adhesion force $F_{H0} = (C_H \cdot r_{1,2})/(6 \cdot a_0^2)$ (2). This is the so called jump-in [see Eq. (1)]

$$F_N\,(h_K)_{approach} = -\frac{F_{H0} \cdot a_0^2}{(a_0 - h_K)^2}. \tag{1}$$

It is worth here that this force is not equilibrated $F_N < 0$. But if the contact is loaded from the point (2) of the adhesion force to the positive yield point (4), it is elastically deformed (3) with an approximated circular contact area according to Hertz [8] and Derjaguin [12] (with adhesion) [see Eq. (2)]

$$F_N\,(h_K)_{elastic} = \frac{2}{3} \cdot E^* \cdot \sqrt{r_{1,2} \cdot h_K^3} - F_{H0}. \tag{2}$$

The effective radius $r_{1,2}$ characterizes the average surface curvature before contact flattening. The effective modulus of elasticity E* results from the series connection of the two elastic elements. When the Hertz curve intersects the abscissa, the total force equilibrium within the self equilibrating contact is obtained. By increasing the external normal load, the soft contact starts at the micro-yield strength with plastic yielding at this point (4). There is the transition from elastic to elastic-plastic deformation [1,22,23]. The displacement at this point (4) is given by Eq. (3)

$$h_{K,Y} = r_{1,2} \cdot \left(\frac{3 \cdot \pi \cdot p_f \cdot (\kappa_A - \kappa_p)}{2 \cdot E^*} \right)^2. \tag{3}$$

The yield pressure p_f (contact yielding) is due to stronger solid (covalent, metallic or ionic) bonds within particle matter. The displacement dependent elastic-plastic contact area ratio κ_A [Eq. (4)] describes the contribution of the circular inner plastic contact area A_{pl} to total contact area A_K including an annular elastic deformation and is based on the force equilibrium [24].

$$\kappa_A = \frac{2}{3} + \frac{1}{3} \cdot \frac{A_{pl}}{A_K}. \tag{4}$$

By inserting the surfaces of the contact circles in Eq. (4), we obtain the relation for the contact area ratio, which affects the loading in normal direction, see Eq. (5)

$$\kappa_A = 1 - \frac{1}{3} \cdot \left(\frac{h_{K,Y}}{h_K}\right)^{\frac{1}{3}} = \frac{2}{3} \cdots 1. \tag{5}$$

For an ideal elastic deformation κ_A is equal to 2/3, for perfectly plastic deformation $\kappa_A = 1$. κ_P is the plastic repulsion coefficient [Eq. (6)], which depends on the van der Waals bond stress p_{VdW} within the contact area and the yield pressure at particle surface p_f.

$$\kappa_P = \frac{p_{vdW}}{p_f} = \frac{C_{H,sls}}{6 \cdot \pi \cdot a_0^3 \cdot p_f} = \frac{4 \cdot \gamma_{sls}}{a_0 \cdot p_f}, \tag{6}$$

with $C_{H,sls}$ values in a range from 0.2 to $40 \cdot 10^{-20}$ J (index sls: van der Waals interactions between two solid surfaces with interstitial adsorbed water molecules), $p_{vdW} \approx 3 - 600$ MPa [1] and a surface energy of $\gamma_{sls} \approx 0.25 - 50\,\mathrm{mJ/m^2}$ from Eq. (6) for diverse particle matter. The effective normal force for a particle-particle contact with adhesion (5) corresponds to a microscopic characteristic stress limit function [see Eq. (7)] [24]

$$F_N\,(h_K)_{elastic-plastic} = \pi \cdot r_{1,2} \cdot p_f \cdot (\kappa_A - \kappa_p) \cdot h_K - F_{H0}. \tag{7}$$

The slope correlates to the elastic-plastic contact stiffness $k_{N,el-pl}$. Particles that show a soft and compliant contact behavior have a low slope. A steep force-displacement behavior symbolizes a stiff contact. The adhesion limit (8) with negative normal or pull-off force $F_N < 0$ characterizes also a characteristic stress limit function and specifies all possible detachment points $h_{K,A}$, see Eq. (8). The slope of this function indicates the adhesive stiffness which depends on the plastic stiffness consider $p_{vdW} = \kappa_P \cdot p_f$. A large negative slope stands for a soft contact behavior. With a stiff contact in addition to a low slope $\kappa_P \ll 1$ an almost constant adhesion or pull-off force is characteristic $F_N \approx -F_{H0}$. The elastic domain is located between the elastic-plastic yield limit and the adhesion limit

$$F_N\,(h_K)_{adh.limit} = -\pi \cdot r_{1,2} \cdot p_{VdW} \cdot h_K - F_{H0}. \tag{8}$$

Any normal loading yields an increasing displacement. But if the contact would be unloaded (6), beginning at an arbitrary point $h_{K,U}$, the elastically deformed, annular contact zone would be recovered along a parabolic curve [see Eq. (9)]

$$F_{N\,unload} = \frac{2}{3} \cdot E^* \cdot \sqrt{r_{1,2} \cdot (h_K - h_{K,A})^3} - F_{HA}, \tag{9}$$

with the adhesion force F_{HA} and the displacement $h_{K,A}$ at the adhesion limit function.

The reloading curve (7) [see Eq. (10)] would run along an equivalent curve from the adhesion limit to the elastic-plastic yield limit

$$F_{N\,reload} = -\frac{2}{3} \cdot E^* \cdot \sqrt{r_{1,2} \cdot (h_{K,U} - h_K)^3} + \pi \cdot p_f \cdot r_{1,2} \cdot (\kappa_A - \kappa_P) \cdot h_{K,U} - F_{H0}. \tag{10}$$

This hysteresis follows from the energy absorption or dissipation W_{diss} of the elastic-plastic contact, which is assumed as a lenticular area between unloading and reloading curve (described by Antonyuk et al. [26] for granules) [see Eq. (11)]

$$W_{diss} = \int_{h_{K,A}}^{h_{K,U}} F_{N,reload}(h_K)\, dh_K - \int_{h_{K,A}}^{h_{K,U}} F_{N,unload}(h_K)\, dh_K. \tag{11}$$

If the adhesion limit is reached, the contact planes detach with an increasing surface distance (9). This particle separation can be considered for the calculation by means of a short range hyperbolic adhesion force curve [see Eq. (12)]

$$F_N(h_K)_{detach} = -\frac{F_{H0} \cdot a_0^2}{(a_0 + h_{K,A} - h_K)^2} - \frac{\pi \cdot r_{1,2} \cdot \kappa_P \cdot p_f \cdot h_{K,A}}{(a_0 + h_{K,A} - h_K)^3} \cdot a_0^3. \tag{12}$$

At a few nanometers surface distance $-h_K$ the normal force approach nearly zero $F_N \approx 0$.

3 Experimental setup

In this section the surface treatment and functionalization of the micro glass particles will be discussed. Subsequently, a description of the determination of the microscopic particle properties by atomic force microscopy (AFM) and nanoindentation measurements is mentioned. For the measurements of the macroscopic contact behavior of cohesive bulk materials the method of ring shear cell testing is used.

3.1 Functionalization and characterization

In aqueous medium, depending on the pH, the unmodified glass particles have polar functional groups on their surfaces (Si–O^-, Si–OH and Si–OH_2^+) [7]. These polar groups can interact with water molecules, whereby the water–surface interaction forces exceed the cohesive forces of bulk water [27]. Those surfaces are called hydrophilic, because this interaction causes the water to spread on the surface. The

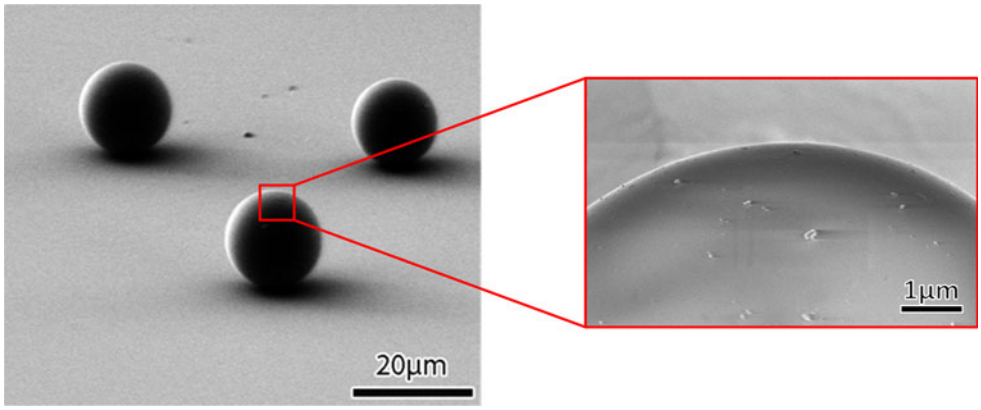


Fig. 2 SEM micrograph of smooth surfaces of unmodified glass particles

surface hydrophobization is possible by means of a so-called silanization. In that case the hydrophobic surface is achieved by replacing the polar groups with non-polar organic rests [27]. Hereby the surface energy of the treated substrate is lowered and the water–surface interaction forces are not large enough to compensate the cohesion forces of bulk water. In this case the water remains as droplet on the surface.

The organosilanes are silicon chemicals that possess reactive hydrolysable groups and inert organic rests [27]. The hydrolysable groups (usually hydroxy (∼OH), chlorine (∼Cl), alkoxy ($\sim OC_nH_{(n+3)}$) [28]) react with the hydroxyl groups, present on the particles surface after a prior surface cleaning and activation process [29]. The functional groups are attached through stable covalent (siloxane) bonds to the particle surface [30].

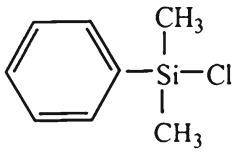
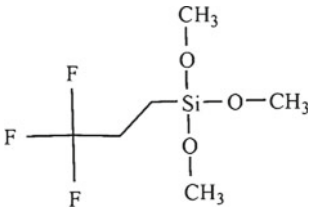
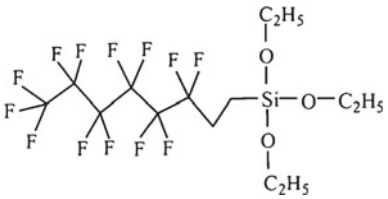
Smooth glass particles are used in the present study (Spheriglass® 5000 CP00, Potters Europe GmbH) to minimize the smear effect of surface asperities. Initially, the particles had the following volume fraction based size distribution, measured with laser diffraction spectroscopy (Mastersizer 2000, Malvern Instruments): $d_{10} = 3.5\,\mu m$, $d_{50} = 10.7\,\mu m$ and $d_{90} = 21.5\,\mu m$. However, prior to modification the small particles were separated by sieving through a 10 µm micro-sieve with ALPINE Air Jet Sieve e200 LS, to separate fine fraction and achieve a narrower size distribution. The median particle size after this sample preparation was $d_{50} = 17.3\,\mu m$. The used particles are nonporous, have a smooth surface and contain approximately 73 % SiO_2. In Fig. 2 SEM-micrograph of the used glass particles is shown. On the surface of the particles some small fragments and contaminations can be observed. They are a result from the stressing at industrial production process. Therefore, before the modification process, the particles were cleaned and at the same time also activated by a chemical cleaning process with peroxymonosulfuric acid. This acid is a mixture of concentrated (95–97 %) sulfuric acid (H_2SO_4) and concentrated (50 %) hydrogen peroxide (H_2O_2) in ratio 3:1. It is a very strong oxidizing agent, which removes the organic residues and activates (hydroxylates) the surface [31]. This process was used to produce the hydrophilic particles. After the pretreatment the particles were modified, using three different silanes: Chlorodimethylphenylsilane (CDMPS), 3,3,3-Trifluoropropyltrimethoxysilane (FPTS) and 1H,1H,2H,2H-Perfluorooctyltriethoxysilane (PFOTES), see Table 3.

Methanol was used as a solvent in the wet-chemical silanization process. The amount of the modifying agent was chosen to be sufficient to build a monolayer on the particle surface. The reaction mixture was stirred for 5 h and then heated up to evaporate the solvent and washed up several times with the solvent, to remove any physisorbed molecules. Finally, the particles were dried in an oven for 12 h at a temperature of 70 °C.

The wettability of the modified and unmodified particles was experimentally tested with water droplet and the result comparison verified the effective surface modification. Further, the surface modification was established by Fourier transform infrared spectroscopy (FTIR) (Fig. 3). The FTIR spectra clearly indicate the attachment of the organic rests to the particles surface [32]. The spectra also show that not all of the hydroxyl groups were changed during the modification process. This can be due to the inhomogeneity of the amorphous glass and the irregular distribution of the OH-groups on the surface. This means that the surface is not fully covered with a monolayer.

The next step of the characterization process was to quantify the hydrophobicity degree in terms of static contact angle measurements with the sessile drop technique [33]. It is an optical method which measures the contact angle which is formed on the three-phase contact of the liquid and solid and the surrounding them vapor or gas phase (Fig. 4). Due to the small particle size, it was not possible to measure directly the contact angle on the particle surface. For this purpose, as a model system, glass slides with the same chemical composition as the glass particles were used. The contact angles were measured with an OCA 15plus instrument (Data Physics Instruments GmbH). The largest contact angle was measured on the surface modified with PFOTES, which is

Table 3 Chemical properties of the modifying agents

Compound	Molecular structure	Molar mass (g/mol)	Density [g/cm^3] 25 °C
Chlorodimethylphenylsilane (CDMPS)		170.71	1.02
3,3,3-Trifluoropropyl trimethoxysilane (FPTS)		218.25	1.14
1H,1H,2H,2H-Perfluorooctyl triethoxysilane (PFOTES)		510.36	1.33

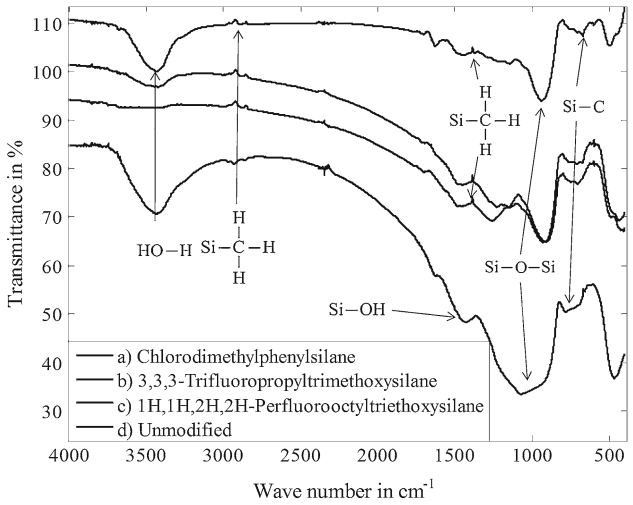


Fig. 3 Fourier transform infrared absorption spectra (FTIR) of the glass particles

due to its long hydrophobic fluorocarbon chain. Due to the hydroxyl groups present on the surface, the lowest contact angle (lower than 10°) was measured on the surface cleaned with peroxymonosulfuric acid (Fig. 4).

With the help of these measurements a model-based calculation of the free surface energy of the unmodified and modified glass slides was accomplished. Although the surface energy was calculated only for a model system, it shows the tendency how it changes after the modification. The surface energy of liquids and solids, γ, consists of polar γ_P and dispersive molecule fraction γ_D of van der Waals interactions. The polar component of the surface energy is due to the dipole–dipole interactions, hydrogen bonds and acid-base interactions [34]. The dispersive component γ_D results from the non-polar molecule interactions [34]. To calculate the surface energy, contact angle measurements with two referent liquids (with known polar and dispersive components), water and α-bromnaphthalene, were conducted.

For the calculations the OWRK model [35] as the well suited model for complex interactions was used. The results clearly show a decrease of the surface energy for the hydrophobic surface and an increased surface energy in case of the hydrophilic surface (Fig. 5). The surface hydrophobization with PFOTES and FPTS did not cause only the expected decrease of the polar surface energy component, but has also lowered the dispersive one. The reason for that lies in the fact, that due to the high electronegativity of fluorine, the polarizability of the fluorocarbon molecules is reduced. That results in decreased charge fluctuations (instantaneous dipole inducing), responsible for the non-polar London dispersion forces [36]. One can also see that the dispersive energy of the surface modified with PFOTES is the lowest. This phenomenon was also observed by Lindner and Ariast [37]. They noticed that the dispersion surface energy of substrates modified with fluoroalkyl silanes decreases with increasing length of fluorocarbon chain. The slight increase of the dispersive energy component for the substrate modified with CDMPS is most probably due to measurement errors and requires further studies.

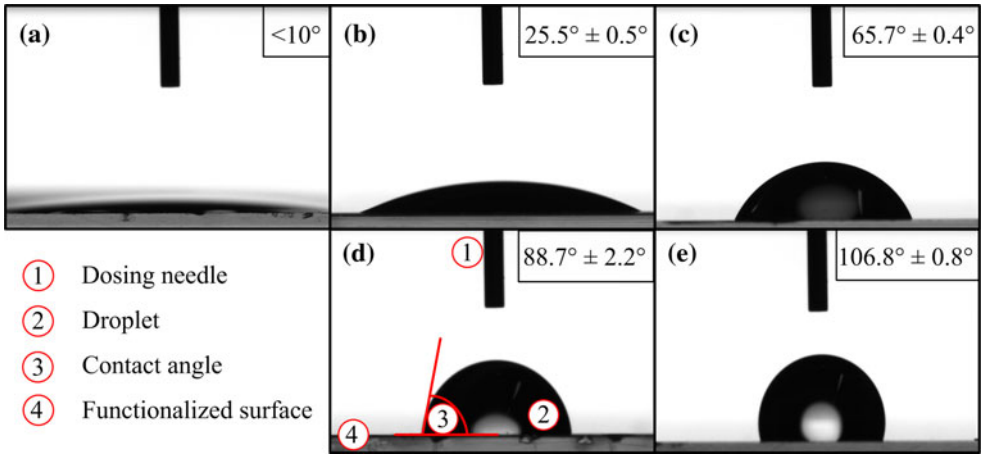


Fig. 4 Static contact angle measurements of glass slides modified with: **a** peroxymonosulfuric acid; **b** unmodified; **c** Chlorodimethylphenylsilane; **d** 3,3,3-Trifluoropropyltrimethoxysilane and **e** 1H,1H,2H,2H-Perfluorooctyltriethoxysilane

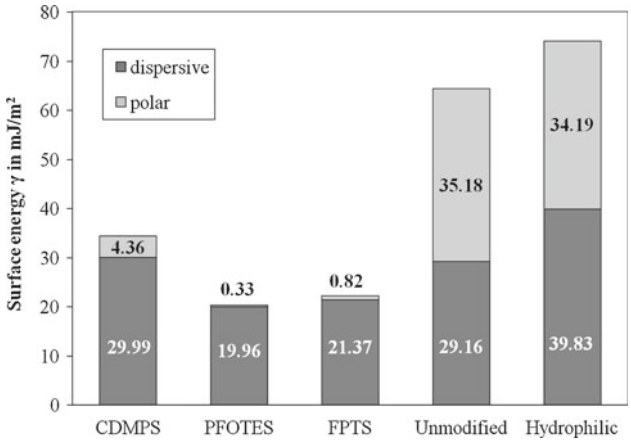


Fig. 5 Surface energy of the glass surface with its polar and dispersive components prior and after the modification

Another interesting observation is that the hydrophilic surface has almost the same polar surface energy as the unmodified one, but the dispersive surface energy has been increased. Therefore, we can expect higher van der Waals forces between the hydrophilic particles and lower between the hydrophobic surfaces.

Since theoretically the layer thickness is in nanometer range, it was not possible to reveal its structure with scanning electron microscopy due to the low resolution. Therefore, the surface layers were measured with non-contact AFM (XE-100, PSIA). Five $2.5 \times 2.5\,\mu m^2$ scans are taken at different surface positions of each sample in order to derive the root mean square (RMS) of layer thickness. Using a plane and line-fit in XEI software (PSIA) the images (Fig. 6) were processed.

Using laser diffraction spectroscopy (Mastersizer 2000) the particle size distribution after modification was measured. The results showed an increased size of particles modified with CDMPS and PFOTES, which indicates an agglomerate formation. The reason for this is the technique used for the silanization. When the solvent was evaporated the unreacted silane was deposited on the particle surface and agglomerates were built.

3.2 Atomic force microscopy

One possibility to determine forces between two macroscopic bodies provides the spring balance method which was already used by Bradley [38] and later by Derjaguin et al. [39], Black et al. [40], Rouweler and Overbeek [41], Israelachvili and Tabor [42,43], Israelachvili and Adams [44] and Israelachvili [25]. This method is not suitable for too small particle sizes [45]. For the determination of the adhesion force of micro-scale particles in contact, the AFM is used. The AFM was invented in 1986 by Binning et al. [46] and is used on the one hand to image high-resolution surface topographies, and on the other to record the force-displacement behavior of particle-particle or particle-wall contacts [47–51]. The measured force curves provide valuable informations about material properties such as adhesion, elasticity and hardness. For this reason, the force-curve measurements are increasingly used in advanced material science and technology [52].

Figure 7 a shows schematically the experimental setup of the used atomic force microscope.

To accomplish direct force-displacement measurements, the method of colloidal probe technique [51] was applied. The measurements were carried out with an atomic force microscope (Asylum Research MFP 3DTM AFM). For all the performed experiments, the ambient air temperature was $23.4 \pm 0.3\,°C$ and the encountered relative humidity was $15.9 \pm 0.7\,\%$. At the end of the AFM cantilever (Fig. 7b), which was used as a force sensor, a micro-sized glass par-

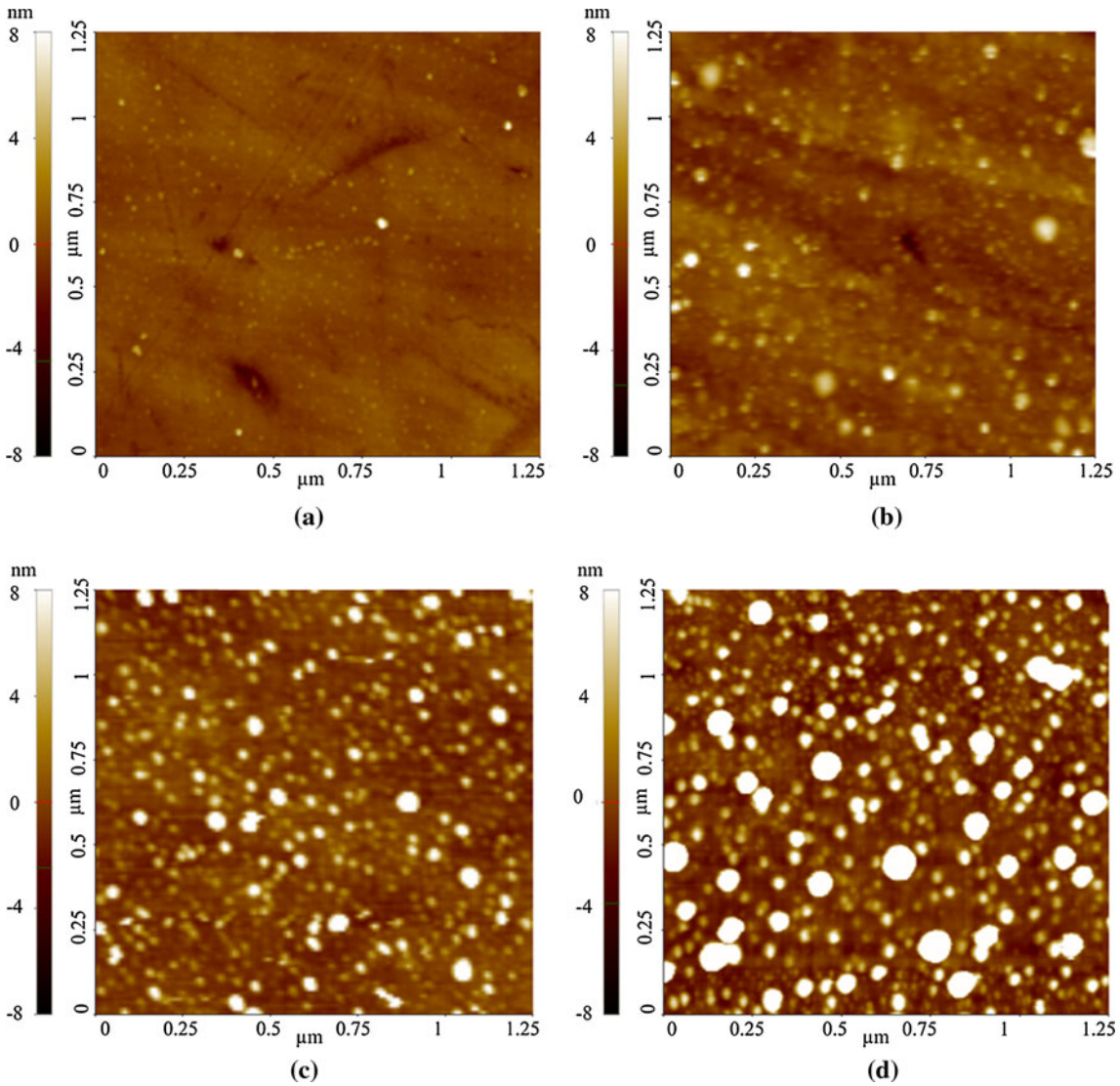


Fig. 6 AFM measurements of the surface topography of a **a** cleaned, hydrophilic glass slide (RMS = 0.8 nm); **b** glass slide modified with CDMPS (RMS = 2.1 nm); **c** glass slide modified with FPTS (RMS = 4.2 nm); **d** glass slide modified with PFOTES (RMS = 11 nm)

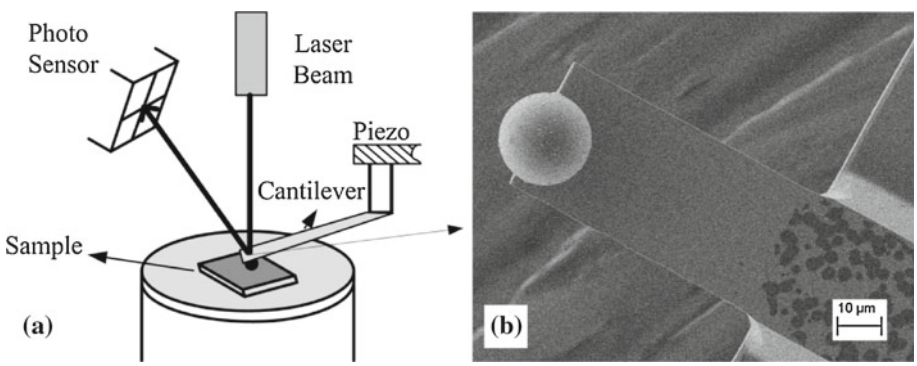


Fig. 7 **a** Principle of the test of atomic force microscopy; **b** scanning electron micrograph of an unmodified micro glass particle, which was glued to the end of a tipless cantilever

ticle was glued. The NSC35/tipless/AlBS cantilever, from Schaefer Technology GmbH, had a length of about 90 μm and a spring constant of 10.47 N/m. The determination of the spring constants of the cantilevers was carried out by the thermal noise method. The micro-glass particles were found to have an average diameter of $d_{50} = 17.3\,\mu m$ and a

surface roughness of 0.8 nm. The exact diameter was determined by a scanning electron microscope. The evaluation of the surface roughness was performed by using a non-contact AFM (XE-100, PSIA). To glue the particle and cantilever together a two-component adhesive (Araldite, epoxy) was used. To investigate the adhesion forces, silica plates were functionalized as described in Sect. 3.1 and the related force-displacement curves via particle-wall contacts were measured. Therefore 10 × 10 points were investigated at three times in a 50 µm × 50 µm area. The velocity of the measurement of the particle-wall contact was 1 µm/s.

3.3 Nanoindentation

Nanoindentation has been used to determine force-displacement curves between two particles or particle and wall to calculate model based the material properties such as modulus of elasticity E and adhesion force F_{H0}. By a certain adaption, the nanoindentation is suitable to characterize the material data of micro-scaled particles [53]. The experiments at the microscopic scale by nanoindentation were performed using TriboIndenter provided by Hysitron Inc. which is shown schematically in Fig. 8.

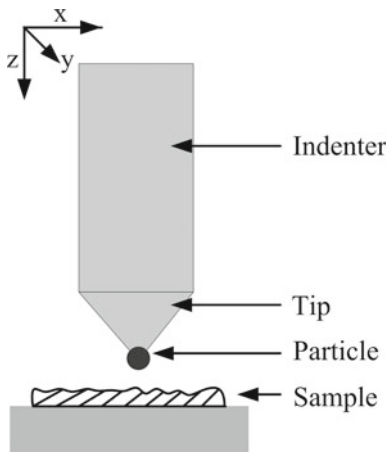


Fig. 8 Schematic representation of experimental setup used to perform the indentation

The method of tip preparation was first published by Fuchs et al. [54]. The following Fig. 9 illustrates the preparation of the tip. A spherical, (cube corner diamond tip; Hysitron Inc.) attached glass particle (d_{50} = 17.3 µm), see Fig. 9a, is used on a three-sided pyramidal tip. In the first step a cavity is cut into the diamond tip (Fig. 9b) by means of a focused ion beam system (FEI Helios 600). The hole appropriated an ideal locating surface for the particle because of its diameter ($d_{hole} < d$). Since the hole-diameter is smaller than the depth of the hole, the contact area between the particle and tip is only formed by a circular ring.

Therefore, the contact between tip and particle does not affect the measurements negatively. Following this, the particle is attached to the tip with the help of an AFM (XE-100, PSIA) and photosensitive acrylate-based adhesive (DIC Europe GmbH). The AFM is used as a micromanipulator for the positioning of the particle. The evaluation of the quality of prepared tips takes place by using SEM images (Zeiss Ultra 55), see Fig. 9c).

The functionalization was differently accomplished regarding the purification step, which was described in Sect. 3.1. Because of the organic basis of the adhesive the particle was cleaned under oxygen plasma for 30 s. The particle-wall contacts between the glass particle and glass slide were measured displacement-controlled with a preload of 1 µN. The measurements were carried out with unmodified particles on modified surfaces, as well as the contact of mutually functionalized contact partners. The maximum depth of indentation was set to 32 nm. In an area of 50 µm × 50 µm 49 measurements were carried out for three times. For all the performed nanoindentation experiments, the ambient air temperature was 22.8 ± 0.3 °C and the encountered relative humidity was 29.6 ± 0.4 %.

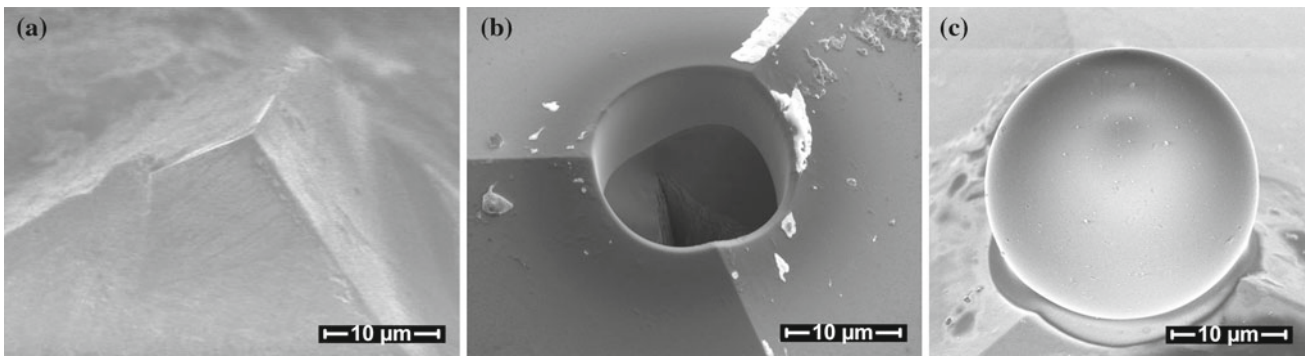


Fig. 9 Scanning electron micrographs; **a** three-sided pyramidal diamond cube corners tip (Hysitron Inc.) [55], **b** cut hole by means of focused ion beam, **c** attached glass particle (adhesive glue: DIC Europe GmbH)

3.4 Shear tester

The flowability of the modified and unmodified particles was measured with a Schulze Ring shear cell apparatus RST-XS in a standard shear cell XS-Mr with a specimen volume of 30 ml [56]. With the shear tester the stresses are measured which lead to flow or irreversible plastic shear deformation [57]. The yield stress as a function of the applied normal stress is called yield locus and cannot be crossed. Two or more yield loci measured at different stresses determine the consolidation function of the powder [58]. According to Jenike [59], the flow function ff_c, is a correlation between the major principal stress σ_1, which is the maximum consolidation stress at the yield locus, and the uniaxial compressive strength σ_c, which represents the powder strength for a certain consolidation stress. The classification of the powder flow behavior according to Jenikes flow function is given by Jenike [59] and Tomas [60].

The yield locus is measured in three steps: preconsolidation, preshear and shear [61]. At first the specimen is compacted applying a pre-consolidation normal stress σ. The second step implies powder shearing, at normal preshear stress σ_{pre}, until reaching the steady state flow, which is a flow under a constant shear stress and constant bulk density at the applied normal force. Then the powder is released from the load. Finally, the measurement continues under reduced normal stress σ that results in smaller shear stress τ with a peak (the last measurement step) when the consolidated powder fails and expands (dilatancy), which is called incipient flow. Beside the flow function and additional powder flow and consolidation characteristics can also be measured with shear tests and they are given in previous publications [58,60,62].

The shear tests were conducted at four preshear stresses: 2, 4, 8 and 16 kPa.

4 Experimental results

To compare single-particle contacts with particle packings the obtained results are presented in this section. While in Sect. 4.1 a description is given of how the model equations are used in order to evaluate the contact properties, in 4.2 the obtained AFM and nanoindentation results are presented and Sect. 4.3 refers to the results of the shear tests.

4.1 Methodology and approach

In the following section the usage of the contact model 'stiff particles with soft contacts' and the model based back-calculation of the material properties are shown and discussed for the force-displacement curves.

If the elastic-plastic yield limit is also a bit curved like the elastic deformation (see Fig. 10a) the abscissa is plotted with the converted displacement $hK^{3/2}$ for a better visibility of the yield point Y and the elastic compression range. Consequently a straight line with the slope a_1 can be achieved, see Fig. 10b.

By means of a linear regression of the measured values $F_N = f(h_K^{3/2})$ and therefore a_1, the effective modulus of elasticity E* results in Eq. (13)

$$E^* = 3 \cdot a_1 \cdot \sqrt{\frac{2}{r_{1,2}}}. \tag{13}$$

The deformation in normal direction leads to a transverse strain of the particle. By means of the Poisson ratio for glass ($\nu = 0.25$) [63] the modulus of elasticity E can be determined as follows, see Eq. (14)

$$E_2 = \frac{1 - \nu_2^2}{2} \cdot E^*. \tag{14}$$

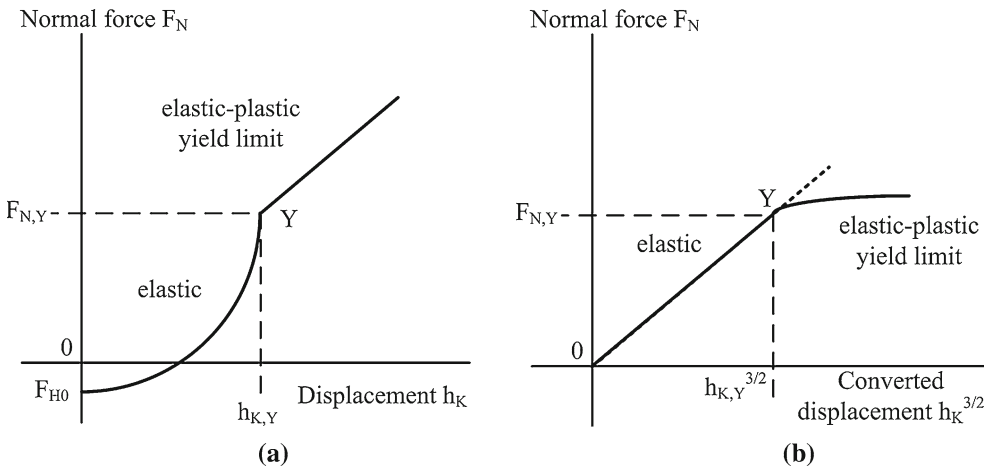


Fig. 10 **a** Normal force-displacement function; **b** linearized normal force-displacement function

Furthermore the force $F_{N,Y}$ and the contact flattening $h_{K,Y} = (h_{K,Y}^{3/2})^{2/3}$ at the yield point Y can be estimated. Through Eq. (15) the mean contact stiffness for loading $k_{N,el,Sec}$ in the elastic range might be approached as secant contact stiffness,

$$k_{N,el,Sec} = \frac{F_{N,Y}}{h_{K,Y}}. \tag{15}$$

Because of the relatively wide elastic deformation range and the obtained significantly high values of the yield limit [26, 64–66], the elastic-plastic yield limit will be determined by Eq. (16)

$$\begin{aligned} F_N(h_K) &= \frac{\pi}{2} \cdot r_{1,2} \cdot p_f \cdot (\kappa_A - \kappa_p) \cdot (h_K - h_{K,Y}) \\ &\quad + F_{N,Y} - F_{H0} \\ &= a_2 \cdot (h_K - h_{K,Y}) + b_2 \end{aligned} \tag{16}$$

Additionally the displacement at yield point $h_{K,Y}$ is used to supplement Eq. (7). The linear regression of the experimentally determined yield limit provides the slope a_2 and the y-intercept b_2. This lead to the characteristic adhesion force F_{H0} with [Eq. (17)]

$$F_{H0} = F_{N,Y} - b_2, \tag{17}$$

to the characteristic micro-yield strength p_f [Eq. (18)]

$$p_f = \frac{E^*}{\pi} \sqrt{\frac{h_{K,Y}}{2 \cdot r_{1,2}}}, \tag{18}$$

the elastic-plastic contact stiffness $k_{N,el-pl}$, see Eq. (19)

$$k_{N,el-pl} = a_2 = \frac{\pi}{2} \cdot r_{1,2} \cdot p_f \cdot (\kappa_A - \kappa_p) \tag{19}$$

and the plastic repulsion coefficient κ_P [Eq. (20)]

$$\kappa_p = \kappa_A - \frac{2 \cdot a_2}{\pi \cdot r_{1,2} \cdot p_f}. \tag{20}$$

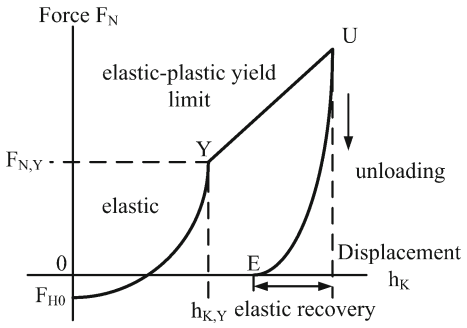


Fig. 11 Force-displacement function of the elastic-plastic contact with unloading

The unloading of the compression test leads to the elastic recovery of the contact, see Fig. 11. The intercept of the abscissa E for $F_N = 0$ describes the residual plastic displacement $h_{K,E}$.

Another important parameter to characterize the increasing adhesion by contact flattening is the contact consolidation coefficient κ. It represents the contact softness at increasing adhesion forces. The elastic-plastic contact consolidation coefficient κ [see Eq. (22)] denotes the current contact stiffness and the increase of the adhesion force F_H [Eq. (21)] with the exposure of a pre-consolidation force F_N [1,24]

$$F_H(F_N) = (1 + \kappa) \cdot F_{H0} + \kappa \cdot F_N \tag{21}$$

and

$$\kappa = \frac{\kappa_p}{\kappa_A - \kappa_p}. \tag{22}$$

A large value of κ shows a soft contact behavior with a high adhesion potential (see Table 2). On contrary a very stiff contact with small adhesion potential is characterized by a very small contact consolidation coefficient $\kappa \approx 0$.

4.2 Single particle contact

4.2.1 Atomic force microscopy

Figure 12 represents the average pull-off forces obtained from the AFM measurements. For each type of surface modification 300 measurements were performed at different areas of the glass slides. The adhesion force was determined by an unmodified glass particle, glued to the cantilever, and the modified or functionalized glass slides.

The largest adhesion force was found for the hydrophilic contact. It amounts to 1.93 µN with a standard deviation

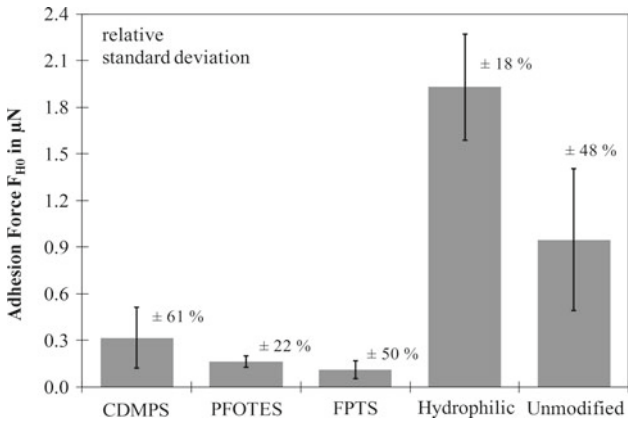


Fig. 12 Results of the adhesion forces determined with AFM for a glass particle ($d_{50} = 17.3$ µm) and functionalized glass slide surfaces. 10 × 10 points were investigated at three times in a 50 µm × 50 µm area on each surface

of 0.34 μN. The reason for this is based on the polarity of the surface groups which accumulate during the purification process with peroxymonosulfuric acid. This means that the attachment of the hydroxyl groups on the glass surfaces increases the van der Waals attraction forces because of the hydrophilicity.

With an increasing non-polarity of the silane groups, the hydrophobicity of the contact increases which results in a decreased measured adhesion force. The large standard deviation for the hydrophilic contact results from the decreasing of reactivity, because of the ambient atmosphere during the measurements. Contrary the large standard deviation for the unmodified substrates follows due to the production process of glass. Thus, for example contaminations or abrasions are attached to the surfaces. The silanes with the fluoroalkyl, e.g. the FPTS, show the lowest adhesion forces with $F_{H0} = 0.11$; μN and PFOTES with $F_{H0} = 0.16$ μN. At the contact angle measurements of the different functionalizations we obtained a contact angle of 88.7 ± 2.2° for FPTS and 106.8 ± 0.8° for PFOTES. They represent the most hydrophobic behavior, hence smallest adhesion forces.

4.2.2 Nanoindentation

The comparison of the normal force-displacement behavior of the averaged values of the three different functionalities is shown in Fig. 13. Unmodified particles were in contact with unmodified, hydrophilic and hydrophobic wall contacts. Exemplary Chlorodimethylphenylsilane (CDMPS) was chosen as a hydrophobic surface.

According to Hertz [8] the elastic contact radius for a displacement $h_K \leq h_{K,Y}$ is given by Eq. (23):

$$r_{K,el} = \sqrt{h_K \cdot r_{1,2}}. \tag{23}$$

This elastic contact radius $r_{K,el}$ characterizes the elastically deformed contact area. For particle-wall contacts, the effective radius $r_{1,2}$ is equal to the particle radius. For the maximum deformation of 32 nm, the elastic contact radius is 0.53 μm. The stiffest particle behavior was found for the unmodified particle-wall contact with a maximum normal force of 750 μN. The hydrophilic contact deformation is similar to the unmodified contact with a maximum force of 600 μN. With observing the unloading curve (zoom-in view in Fig. 13), it can be observed that the plastic deformation of the surface purification with peroxymonosulfuric acid is smaller. The plastic deformation was characterized by the intercept of the unloading curve with the abscissa (see Fig. 11, point E). Permanent plastic deformations of 2.93 and 1.15 nm were found for the unmodified and hydrophilic contacts, respectively.

The hydrophobic contact shows a clear different behavior. The maximum normal force amounts to only 110 μN but a plastic deformation of 18.33 nm was measured. The normal force-displacement curve is characterized by a small slope, indicating a soft contact behavior. The behavior is probably caused by the multi-layer formation on the functionalized glass surface. During the process of silanization a multi-layer formation on the surface is formed which is too thick in comparison to the contact flattening, i.e. the nanoindenter only measures the deformation of the silanized multi-layer.

To compare the nanoindentation measurements with the powder shear tests, single particle measurements must be carried out within the same stress level as the particles experience in bulk tests. The shear tests were performed for four different normal stresses (σ = 2, 4, 8, 16 kPa). It was measured, that for the shear tests the major principal stress σ_1 varies between 3.5 and 40 kPa. To approximate a macro-micro transition the relevant range of normal forces at nanoindentation is calculated by $F_N \approx \sigma_1 \cdot d_{50}^2$ [4,24,58]. In order to perform nanoindentation measurements with particles (median size $d_{50} = 17.3$ μm) and $\sigma_1 = 3.5-40$ kPa, F_N is 1−12 μN. Based on this result the following measurements were carried out in a range of 10 − 20 μN. This range is due to the variability of the nanoindenter.

Figures 14 and 15 show the results for both-sided functionalized contact partners. For Fig. 14 a cyclic loading experiment with the CDMPS modification was investigated. Ten cycles of loading and unloading at the same contact point were measured. The measurements were investigated displacement controlled with a maximum contact deformation

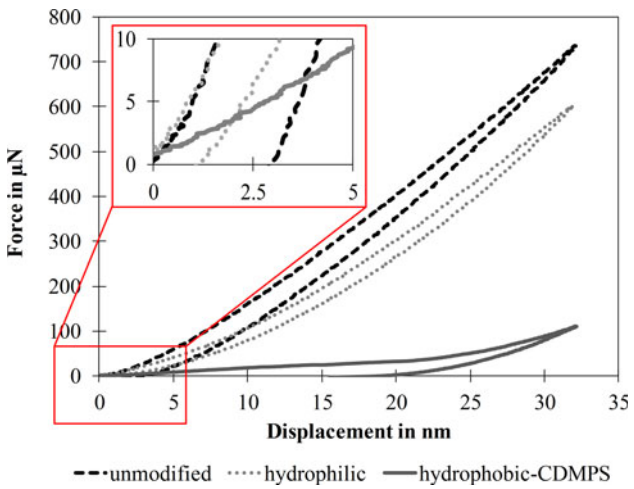


Fig. 13 Comparison of the force-displacement behavior of different modified particles and surfaces (unmodified: untreated glass particle and slide; hydrophilic: treated with oxygen plasma; hydrophobic: functionalized with CDMPS) while measuring a particle-wall contact with nanoindentation. Zoom-in view shows the intercept of abscissa, which describes the area of plastic deformation (displacement controlled: $h_K = 32$ nm, preload: 1 μN)

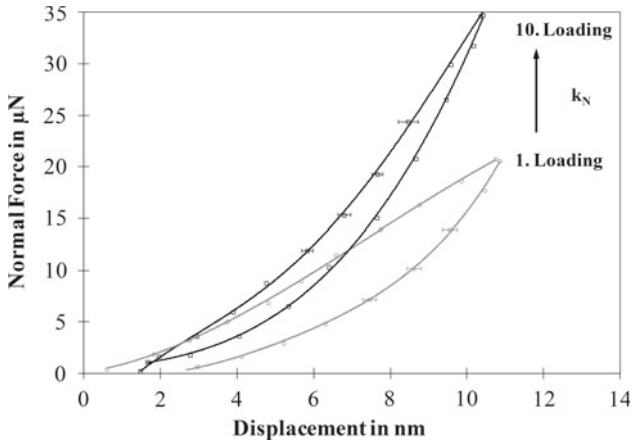


Fig. 14 Fitting of the force-displacement data for a cyclic loading displacement controlled particle-wall contact. Due to clarity only cycle 1 and 10 are shown. Particle and surface were modified with CDMPS. The stiffness increases with the number of cycles. (Cyclic loading: 10 cycles, preload: 1µN)

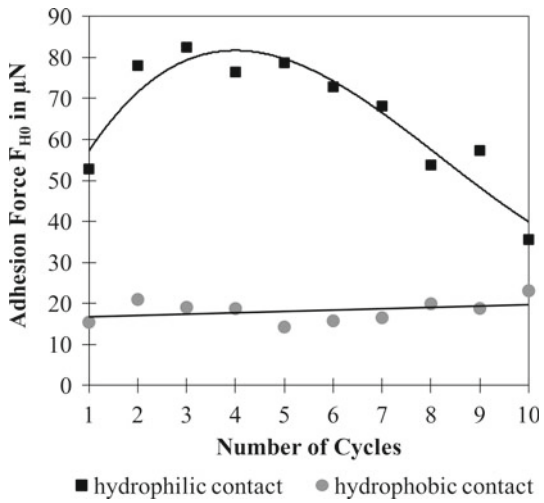


Fig. 15 Comparison of the adhesion forces for 10 cycles of displacement controlled cyclic loading for a hydrophilic and hydrophobic particle-wall contact. (Hydrophilic: treated with oxygen plasma; hydrophobic: treated with CDMPS)

of 11 nm equivalent to an elastic contact radius of 0.31 µm. To simplify Fig. 14, the first and the tenth cycle of the force-displacement curve are shown. It can be observed that an increasing maximum normal force increases with number of cycles. The plastic stiffness, $k_{N,el-pl}$ [Eq. (19)], is the slope of the elastic-plastic yield limit [see straight line (5) in Fig. 1]. We obtained plastic stiffness values of 2.25 and 5.29 N/m for the first and tenth loadings, respectively.

The reason for stiffening behavior is the contact consolidation effect by surface layer yielding and hardening within the contact zone. The contact was deformed more and more plastically to a maximum value was reached. At the first cycle of the measurement the plastic deformation (intercept of the abscissa) was 2.64 nm. In the tenth cycle is an intersection between the loading and unloading curve. This is based on the existing contact flattening at the moment of the 10th measurement. Due to the plastic deformation the contact between the two particles starts later (the starting position of the indenter is for every cycle the same), but no further plastic contact deformation is measurable and so the two curves intersect.

In Fig. 15 the adhesion force-changes of the hydrophobic and hydrophilic particle-wall contacts are shown. The surface purification with oxygen plasma was realized as described in Sect. 3.3. Observing the adhesion forces as a function of the number of cycles no pattern is visible for the hydrophobic contact. On the contrary, we observed the decreasing of the adhesion force after the third cycle by the hydrophilic contact. The reason for this behavior can be attributed to the squeezing of water adsorption layers at ambient atmosphere.

The determination of the adhesion force was considered by the contact model for adhesive particles with the investigated yield limit [see Eq. (17)].

Considering this equation, the adhesion force can be calculated by the intercept of the elastic-plastic yield limit and the appeared force at the yield point. The mean adhesion force was determined versus the ten cycles. The hydrophilic contact showed an adhesion of 65.51 µN in contrast to the mean adhesion force of 18.27 µN for hydrophobic contact (Fig. 15).

Another parameter that was characterized is the contact consolidation coefficient κ [see Eq. (22)]. With a characteristic plastic repulsion coefficient of $\kappa_p = 0.51$ [see Eq. (20)] we got a contact consolidation coefficient of 1.58 for the hydrophobic contact. This indicates an extremely soft contact according to Table 2. For the sake of simplicity the elastic-plastic contact surface ratio κ_A was set constant to 5/6 for the elastic-plastic contact behavior [1,4,24]. The κ for the hydrophilic contact was evaluated to be 0.4 with a plastic repulsion coefficient of 0.22. The particle contact is stiffer for purified particles in comparison to the modified and functionalized surfaces.

4.3 Bulk powder analysis

Figure 16 clearly shows a decreased flowability of the modified glass particles, relative to unmodified glass beads. These results are surprising as theoretically with lower surface energy the bulk powder should be more free flowing. The reason for this lies in the used silanization technique. The silanes are extremely moisture sensitive and tend to partially polymerize and form multi-layers by working with non-water free solvents. Especially for long chain silanes, irregular clusters (like micelles) are formed on the surface. Consequently, a certain non-uniform surfaces coating is produced. During loading process, the silane clusters dominate the first contact and hinder to flow due to shear induced interlock and mutu-

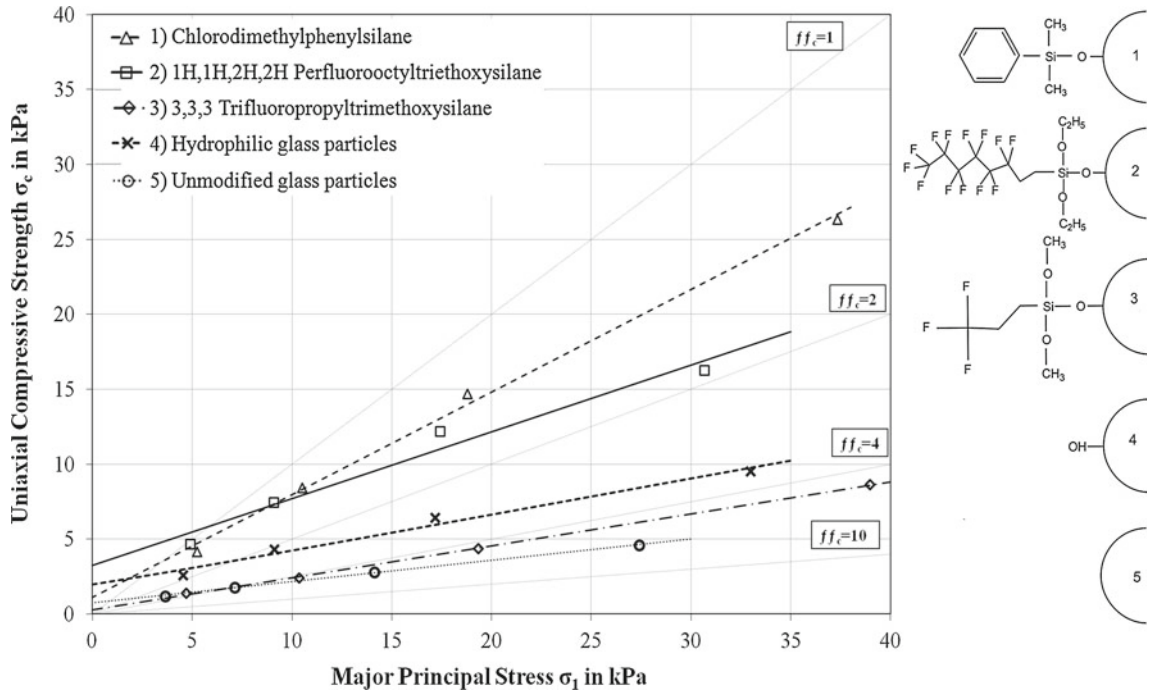


Fig. 16 Macroscopic consolidation function of powders with modified and unmodified glass particles, measured at ambient conditions

ally penetration and association of hydro-carbon chains. This leads to an increased compressive strength and a decreased flowability [62]. Therefore the modification process has to be continued and optimized.

The cleaned (hydrophilic) particles also have a lower flowability than the unmodified particles. This is related to the increased surface energy (Fig. 5) and therefore the increased adhesion forces (Fig. 12) by water adsorption layers.

By a suitable micro–macro transition for normal/tangential contact forces and normal/shear stresses [4,24,58] using the model 'stiff particles with soft contacts' the micro mechanical particle properties, i.e. the characteristic mean adhesion force between two particles of unconsolidated powder F_{H0}, the elastic-plastic contact consolidation coefficient κ, the plastic repulsion coefficient κ_p and the characteristic load dependent total adhesion force between two particles in contact F_H were back-calculated.

The pressure dependent adhesion force between two particles in contact F_H (Fig. 17) is calculated as a linearized function of the contact normal force F_N (calculated as shown in [4]), the adhesion force without any contact deformation F_{H0} and the elastic-plastic contact consolidation coefficient κ [Eq. (21)] [58].

The slope of the adhesion force characterizes the contact consolidation coefficient κ [1] (Table 2) e.g. the higher the slope, the more compliant is the contact and vice versa the lower the slope the stiffer is the contact. The particles modified with CDMPS show the largest adhesion force F_H increase with an increasing normal force F_N, i.e. the largest slope κ.

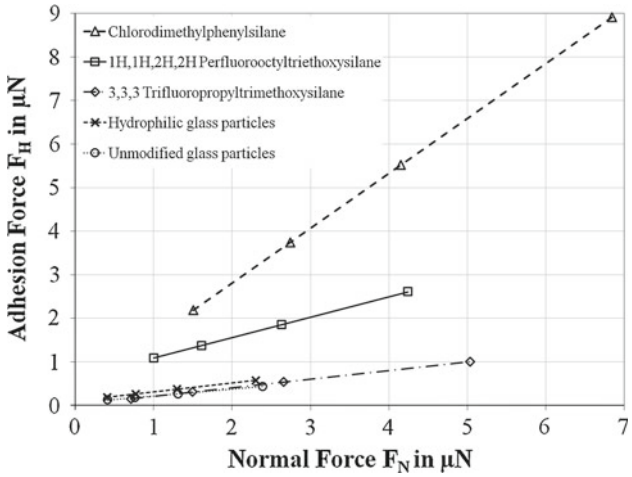


Fig. 17 Microscopic characteristic adhesion force versus normal force of the studied micro glass particles back-calculated from shear tests

On Fig. 18a, the attractive adhesion force F_{H0} (the adhesion force without any contact flattening) is shown. The results for the unmodified, hydrophilic and hydrophobic particles modified with FPTS are in good agreement with the AFM results (Fig. 12). In case of the modification with CDMPS and PFOTES cannot be determined for sure if the higher adhesion forces are due to the surface structure or due to the agglomerate formation. Figure 18b shows the elastic-plastic consolidation coefficient κ back-calculated from the shear tests.

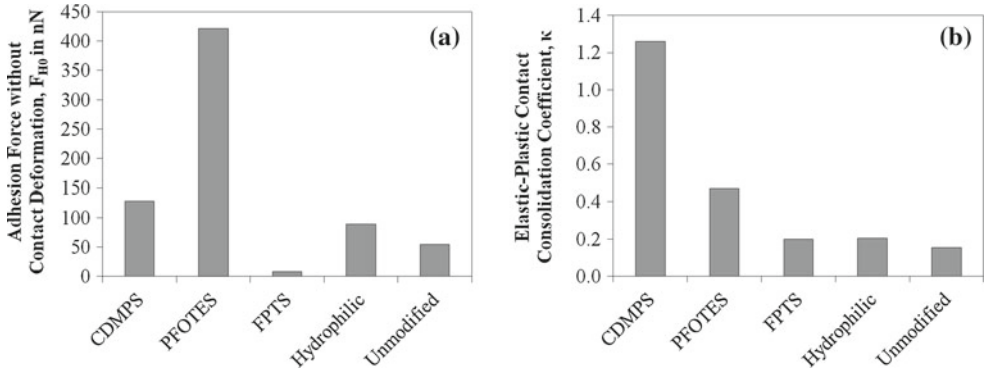


Fig. 18 **a** Characteristic mean adhesion force between two particles of unconsolidated powder F_{H0}; **b** elastic-plastic contact consolidation coefficient κ of the unmodified and the modified particles

Table 4 Comparison of the results from single particle contacts and particle packing measurements

	Nanoindentation			Shear tests		
	CDMPS	Un modified	Hydrophilic	CDMPS	Un modified	Hydrophilic
Adhesion force F_{H0} in μN	18.27	3.80	65.51	0.13	0.055	0.089
Contact consolidation coefficient κ	1.58	0.03	0.37	1.26	0.15	0.20

One can see that the hydrophilic particles show softer contacts as the hydrophobic FPTS particles (Fig. 18b). This is very likely due to the fact that the measurements were carried out under ambient conditions and there are, for sure, water molecules adsorbed on the activated surface, which results in softer contacts and larger adhesion potential.

The particles modified with CDMPS have the softest contact. The reason is probably because of the regular structure of these surface layers after the modification. When the particles are consolidated, the aromatic rings (Table 3) can interlock with each other, which results in higher adhesion forces. That is most likely the reason why these particles have lower attractive adhesion forces then the PFOTES particles, but after contact deformation their adhesion increases.

The calculation of the bulk density of the modified particles shows, that among all the modified particles, the ones modified with FTPS have the largest bulk density. That is because by reducing the adhesion force the rearrangement of the particles into a denser packing encouraged. Contrary, the particles treated with CDMPS, have the lowest bulk density due to the highest adhesion force [62].

5 Conclusion

An extensive analysis of the micro and macro mechanical properties of smooth unmodified, hydrophilic and hydrophobic micro glass particles was accomplished on the basis of the model 'stiff particles with soft contacts'. For the production of the hydrophilic particles a chemical cleaning process and for the hydrophobic—a wet chemical silanization process were used. The micro mechanical contact properties for single particle contacts were measured directly by means of nanoindentation and AFM, and for bulk powder back-calculated from the shear tests. The nanoindentation measurements were conducted at cyclic loading at stress ranges similar to those from the shear tests, in order to compare microscopically between single particle and powder continuum (particle packing).

Table 4 shows a comparison of the model-based back-calculated attractive adhesion force F_{H0} and the elastic-plastic contact consolidation coefficient κ for nanoindentation and shear tests. Due to the utilized silanization technique, which resulted as a non-uniform surface coating, a cluster formation was observed in case of modification with CDMPS. Thus, although the particles treated with these silanes have a lower surface energy after modification, they have an increased adhesion forces and the highest adhesion force calculated from the shear tests lies between the CDMPS modified particles. The highest adhesion forces were measured for hydrophobic particles by nanoindentation. The nanoindenter experiments are conducted for particle-wall contact, which results in a larger contact area after deformation. That is most probably the reason for the higher adhesion forces measured in this case.

The contact stiffnesses determined for one representative contact between two particles from the bulk solid and single particles are in the same stiffness ranges. In both cases the

most compliant contact is measured for the CDMPS and the stiffest for the unmodified particles. Since the van der Waals attraction force is the main reason for adhesion of fine, dry, micro scale particles, we can observe the same tendency for adhesion force change from AFM and surface energy measurements. But the adhesion forces F_{H0} between two particles, measured directly and model based back-calculated from shear tests differ significantly from each other (Table 4) and the comparison between them is still a challenge. Therefore, an optimization of the modification process is needed in order to avoid over dosage and cluster formation of surfactants and coatings.

Generally, it can be concluded, that comparing the two methods, single particle contacts and particle packings are obtained the same contact behavior for the unmodified, hydrophilic and hydrophobic particles.

This study will continue with further nanoindenter investigations at cyclic loading for the hydrophobic particles, modified with PFOTES and FPTS.

Acknowledgments We would like to acknowledge the financial support of the German Research Foundation (DFG) through the priority program 'PiKo – Particles in Contact'.

References

1. Tomas, J.: Adhesion of ultrafine particles—a micromechanical approach. Chem. Eng. Sci. **62**, 1997–2010 (2007)
2. Borho, K., Polke, R., Wintermantel, K., Schubert, H., Sommer, K.: Produkteigenschaften und Verfahrenstechnik. Chemie Ingenieur Technik **63**, 792–808 (1991)
3. Rumpf, H.: Grundlagen und Methoden des Granulierens. Chemie Ingenieur Technik **30**, 144–158 (1958)
4. Tomas, J.: Produkteigenschaften ultrafeiner Partikel—Mikromechanik, Fließ-und Kompressionsverhalten kohäsiver Pulver. Abhandlungen der Sächsischen Akademie der Wissenschaften zu Leipzig, Technikwissenschaftliche Klasse **1**(3), 1–46 (2009)
5. Tomas, J., Kleinschmidt, S.: Improvement of flowability of fine cohesive powders by flow additives. Chem. Eng. Technol. **32**, 1470–1483 (2009)
6. Tomas, J.: Assessment of mechanical properties of cohesive particulate solids—part 1: particle contact constitutive model. Part. Sci. Technol. **19**, 95–110 (2001)
7. Plueddemann, E.P.: Silane Coupling Agents. Plenum Press, New York (1991)
8. Hertz, H.: Über die Berührung fester elastischer Körper. Journal Reine und Angewandte Mathematik **92**, 156–171 (1882)
9. Huber, M.T.: Zur Theorie der Berührung fester elastischer Körper. Annalen der Physik **14**, 153–163 (1904)
10. Lurje, A.I.: Räumliche Probleme der Elastizitätstheorie. Akademieverlag, Berlin (1963)
11. Sperling, G.: Eine Theorie der Haftung von Feststoffteilchen an Festkörpern. Dissertation, TH Karlsruhe (1964).
12. Derjaguin, B.V.: Untersuchungen über die Reibung und Adhäsion, IV—Theorie des Anhaftens kleiner Teilchen. Kolloid Zeitschrift **69**, 155–164 (1934)
13. Derjaguin, B.V., Muller, V.M., Toporov, U.P.: Effect of contact deformations on the adhesion of particles. J. Colloid Interface Sci. **53**, 314–326 (1975)
14. Dahneke, B.: The influence of flattening on the adhesion of particles. J. Colloid Interface Sci. **40**, 1–13 (1972)
15. Dahneke, B.: Further measurements of the bouncing of small latex spheres. J. Colloid Interface Sci. **51**, 58–65 (1975)
16. Johnson, K.L.: Contact Mechanics. Cambridge University Press, Cambridge (1985)
17. Johnson, K.L., Kendall, K., Roberts, A.D.: Surface energy and the contact of elastic solids. Proc. R. Soc. A **324**, 301–313 (1971)
18. Greenwood, J.A.: Adhesion of elastic spheres. Proc. R. Soc. A **453**, 1277–1297 (1997)
19. Götzinger, M., Peukert, W.: Particle adhesion force distributions on rough surfaces. Langmuir **20**, 5298–5303 (2004)
20. Zhou, H., Peukert, W.: Modelling adhesion forces between deformable bodies by FEM and Hamaker summation. Langmuir **24**, 1459–1468 (2008)
21. Li, Q., Rudolph, V., Peukert, W.: London-van der Waals adhesiveness of rough particles. Powder Technol. **161**, 248–255 (2006)
22. Lifshitz, E.M.: The theory of molecular attractive forces between solids. Sov. Phys. (JETP) **2**, 73–83 (1956)
23. Hamaker, H.C.: The London—van der Waals attraction between spherical particles. Physica **4**, 1058–1072 (1937)
24. Tomas, J.: Assessment of mechanical properties of cohesive particulate solids—part 2: powder flow criteria. Part. Sci. Technol. **19**, 111–129 (2001)
25. Israelachvili, J.N.: Intermolecular and Surface Forces. Academic Press, London (1992)
26. Antonyuk, S., Heinrich, S., Tomas, J., Deen, N.G., van Buijtenen, M.S., Kuipers, J.A.M.: Energy absorption during compression and impact of dry elastic-plastic spherical granules. Granul. Matter **12**, 15–47 (2010)
27. Arkles, B.: Hydrophobicity and Hydrophilicity and Silane Surface Modification. Gelest Inc, Morrisville (2011)
28. Butt, H.-J., Graf, K., Kappl, M.: Physics and Chemistry of Interfaces. WILEY-VCH, Weinheim (2006)
29. Liu, X.M., Thomason, J.L., Jones, F.R.: The concentration of hydroxyl groups on glass surfaces and their effect on the structure of silane deposits. In: Silanes and Other Coupling Agents, Brill NV, Leiden (2009)
30. Witucki, G.L.: A silane primer: chemistry and applications of alkoxy silanes. J. Coat. Technol. **65**, 57–60 (1993)
31. Jradi, K., Daneault, C., Chabot, B.: Chemical surface modification of glass beads for the treatment of paper machine process waters. Thin Solid Films **519**, 4239–4245 (2011)
32. Hedge, N.D., Hirashima, H., Rao, A.V.: Two step sol-gel processing of TEOS based hydrophobic silica aerogels using trimethylethoxysilane as a co-precursor. J. Porous Mater. **14**, 165–171 (2007)
33. KRÜSS GmbH: Krüss Advancing Surface Science. http://www.kruss.de/en/theory/measurements/contact-angle/contact-angle.html [Accessed 02 12 2012]
34. Meichsner, G., Mezger, T., Schröder, J.: Lackeigenschaften Messen und Steuern. Vincentz Network GmbH & Co KG, Hannover (2003)
35. Janssen, D., De Palma, R., Verlaak, S., Heremans, P., Dehaen, W.: Static solvent contact angle measurements, surface free energy and wettability determination of various self-assembled monolayers on silicon dioxide. Thin Solid Films **515**, 1433–1438 (2006)
36. Lemal, D.M.: Perspective on fluorocarbon chemistry. J. Org. Chem. **69**, 1–11 (2004)
37. Lindner, E., Ariast, E.: Surface free energy characteristics of polyfluorinated silane films. Langmuir **8**, 1195–1198 (1992)
38. Bradley, R.S.: The cohesive force between solid surfaces and the surface energy of solids. Philos. Mag. **13**, 853–862 (1932)
39. Derjaguin, B.V., Abrikosova, I.I., Lifshitz, E.M.: Direct measurement of molecular attraction between solids separated by a narrow gap. Q. Rev. Chem. Soc. **10**, 295–329 (1956)

40. Black, W., de Jongh, J.G.V., Overbeek, J.T.G., Sparnaay, M.J.: Measurements of retarded van der Waals forces. Trans. Faraday Soc. **56**, 1597–1608 (1960)
41. Rouweler, G.C.J., Overbeek, J.T.G.: Dispersion forces between fused silica objects at distances between 25 and 350 nm. Trans. Faraday Soc. **67**, 2117–2121 (1971)
42. Israelachvili, J.N., Tabor, D.: The measurement of the van der Waals dispersion forces in the range 1.5 to 130 nm. Proc. R. Soc. Lond. **A**(331), 19–38 (1972)
43. Israelachvili, J.N., Tabor, D.: van der Waals forces: theory and experiment. In: Danielli, J.F., Rosenberg, M.D., Cadenhead, D.A. (eds.) Progress in surface and membrane science vol. 7, pp. 1–55. Academic Press, New York (1973)
44. Israelachvili, J.N., Adams, G.E.: Measurements of the forces between two mica surfaces in aqueous electrolyte solutions in the range 0–100 nm. J. Chem. Soc. Faraday Trans. **1**(74), 975–1001 (1978)
45. Tykhoniuk, R., Tomas, J., Luding, S., Kappl, M., Heim, L., Butt, H.-J.: Ultrafine cohesive powders: from interparticle contacts to continuum behaviour. Chem. Eng. Sci. **62**, 2843–2864 (2007)
46. Binning, G., Quate, C.F., Gerber, C.: Atomic force microscopy. Phys. Rev. Lett. **56**, 930–933 (1986)
47. Meyer, E., Heinzelmann, H., Grötter, P., Jung, T., Hidber, H.R., Rudin, H., Guntherodt, H.J.: Atomic force microscopy for the study of tribology and adhesion. Thin Solid Films **181**, 527–544 (1989)
48. Weisenhorn, A.L., Hansma, P.K., Albrecht, T.R., Quate, C.F.: Forces in atomic force microscopy in air and water. Appl. Phys. Lett. **54**, 2651–2653 (1989)
49. Butt, H.-J., Jaschke, M., Ducker, W.A.: Measuring surface forces in aqueous solution with the atomic force microscope. Bioelectrochem. Bioenergy **381**, 91–201 (1995)
50. Capella, B., Dietler, G.: Force-distance curves by atomic force microscopy. Surf. Sci. Rep. **34**, 1–104 (1999)
51. Kappl, M., Butt, H.-J.: The colloidal probe technique and its application to adhesion force measurements. Part. Part. Syst. Charact. **19**, 129–143 (2002)
52. Butt, H.-J., Capella, B., Kappl, M.: Force measurements with the atomic force microscope: technique, interpretation and applications. Surf. Sci. Rep. **59**, 1–152 (2005)
53. Fisher-Cripps, A.C.: Nanoindentation. Springer, New York (2011)
54. Fuchs, R., Meyer, J., Staedler, T., Jiang, X.: Sliding and rolling of individual micrometre sized glass particles on rough silicon surfaces. Tribology **7**(2), 103–107 (2013)
55. Hysitron. Inc.: Tip Selection Guide. http://hysitron.com/LinkClick.aspx?fileticket=bcq5arPC_GE%3d&tabid=429 [Accessed 25 07 2013]
56. Schulze, D.: Schüttgutmesstechnik. http://www.dietmar-schulze.de/leaflxse.pdf [Accessed 01 06 2012]
57. Hintz, W., Antonyuk, S., Schubert, W., Ebenau, B., Haack, A., Tomas, J.: Determination of physical properties of fine particles, nanoparticles and particle beds. In: Tsotsas, E. (ed.) Modern Drying Technology: Experimental Techniques, 2, Wiley-VCH, Weinheim (2009)
58. Tomas, J.: Fundamentals of cohesive powder consolidation and flow. Granul. Matter **6**, 75–86 (2004)
59. Jenike, A.W.: Storage and Flow of Solids. Engineering Experiment Station, vol. 123, University of Utah, Utah (1964)
60. Tomas, J.: Product design of cohesive powders mechanical properties, compression and flow behavior. Chem. Eng. Technol. **27**, 605–618 (2004)
61. Schulze, D.: Zur Fließfähigkeit von Schüttgütern—Definition und Messverfahren. Chemie Ingenieur Technik **67**(1), 60–68 (1995)
62. Tomas, J., Kleinschmidt, S.: Verbesserung der Fließfähigkeit feiner kohäsiver Pulver durch nanoskalige Fließhilfsmittel. Chemie Ingenieur Technik **81**, 717–733 (2009)
63. Czichos, H., Hennecke, M.: Hütte: Das Ingenieurwissen. Springer, Berlin (2008)
64. Antonyuk, S., Tomas, J., Heinrich, S., Mörl, L.: Breakage behaviour of spherical granulates by compression. Chem. Eng. Sci. **60**, 4031–4044 (2005)
65. Müller, P., Tomas, J.: Compression behavior of moist spherical zeolite 4A granules. Chem. Eng. Technol. **35**(9), 1677–1684 (2012)
66. Müller, P., Seeger, M., Tomas, J.: Compression and breakage behavior of $\gamma - Al_2O_3$ granules. Powder Technol. **237**, 125–133 (2013)